

¹ Detection of slow slip events using wavelet
² analysis of GNSS recordings

³ Ariane Duccellier¹, Kenneth C. Creager², and David A. Schmidt²

⁴ ¹Corresponding author. University of Washington, Department of
⁵ Earth and Space Sciences, Box 351310, 4000 15th Avenue NE
⁶ Seattle, WA 98195-1310, ariane.duccellier.pro@gmail.com

⁷ ²University of Washington, Department of Earth and Space
⁸ Sciences

⁹ **Key points**

- ¹⁰ • We use a wavelet-based signal processing method to detect transients in
¹¹ GNSS data, such as slow slip events.
- ¹² • In Northern Cascadia, there is good agreement between detections of slow
¹³ slip using GNSS data and using tremor data.
- ¹⁴ • The method can be applied as a starting point to identify slow slip without
¹⁵ prior information. New Zealand is shown as an example.

¹⁶ **Abstract**

¹⁷ In many places, tectonic tremor is observed in relation to slow slip and can
¹⁸ be used as a proxy to study slow slip events of moderate magnitude where
¹⁹ surface deformation is hidden in Global Navigation Satellite System (GNSS)
²⁰ noise. However, in subduction zones where no clear relationship between tremor
²¹ and slow slip occurrence is observed, these methods cannot be applied, and we
²² need other methods to be able to better detect and quantify slow slip. Wavelets
²³ methods such as the Discrete Wavelet Transform (DWT) and the Maximal
²⁴ Overlap Discrete Wavelet Transform (MODWT) are mathematical tools for
²⁵ analyzing time series simultaneously in the time and the frequency domain by
²⁶ observing how weighted differences of a time series vary from one period to the
²⁷ next. In this paper, we use wavelet methods to analyze GNSS time series and
²⁸ seismic recordings of slow slip events in Cascadia. We use detrended GNSS
²⁹ data, apply the MODWT transform and stack the wavelet details over several
³⁰ nearby GNSS stations. As an independent check on the timing of slow slip
³¹ events, we also compute the cumulative number of tremor in the vicinity of
³² the GNSS stations, detrend this signal, and apply the MODWT transform.
³³ In both time series, we can then see simultaneous waveforms whose timing
³⁴ corresponds to the timing of slow slip events. We assume that there is a slow
³⁵ slip event whenever there is a positive peak followed by a negative peak in the
³⁶ wavelet signal. We verify that there is a good agreement between slow slip events
³⁷ detected with only GNSS data, and slow slip events detected with only tremor
³⁸ data for northern Cascadia. The wavelet-based detection method effectively
³⁹ detects events of magnitude higher than 6 as determined by independent event
⁴⁰ catalogs (e.g. (Michel et al., 2019)). As a demonstration of using the wavelet
⁴¹ analysis in a region without significant tremor, we also analyze GNSS data from
⁴² New Zealand and detect slow slip events that are spatially and temporally close

⁴³ to those detected previously by other studies.

⁴⁴ 1 Introduction

⁴⁵ Slow slip events are new phenomena discovered in the last two decades in many
⁴⁶ subduction zones thanks to recordings of the displacement of Earth's surface by
⁴⁷ dense Global Navigation Satellite System (GNSS) networks (Vergnolle et al.,
⁴⁸ 2010; Schmidt and Gao, 2010; Jiang et al., 2012; Wallace et al., 2012). As with
⁴⁹ ordinary earthquakes, slow slip events represent slip on a fault, for instance
⁵⁰ the plate boundary between a tectonic plate subducting under another tectonic
⁵¹ plate. However, they take a much longer time (several days to several years) to
⁵² happen relative to ordinary earthquakes. They have a relatively short recurrence
⁵³ time (months to years) compared to the recurrence time of regular earthquakes
⁵⁴ (up to several hundreds of years), allowing scientists to observe and study many
⁵⁵ complete event cycles, which is typically not possible to explore with traditional
⁵⁶ earthquake catalogs (Beroza and Ide, 2011). A slow slip event on the plate
⁵⁷ boundary is inferred to happen when there is a reversal of the direction of motion
⁵⁸ at GNSS stations, compared to the secular interseismic motion. Slow slip
⁵⁹ events have been observed in many places (Beroza and Ide, 2011; Audet and
⁶⁰ Kim, 2016), such as Cascadia (Bartlow, 2020), Nankai (Nishimura et al., 2013),
⁶¹ Alaska (Li et al., 2016), Costa Rica (Jiang et al., 2012), Mexico (Radiguet
⁶² et al., 2012), and New Zealand (Wallace, 2020).

⁶³

⁶⁴ In many places, tectonic tremor is also observed in relation to slow slip, but
⁶⁵ the spatial agreement between tremor and slow slip may vary along the strike of
⁶⁶ the plate boundary (Hall et al., 2018). Tremor is a long (several seconds to many
⁶⁷ minutes), low amplitude seismic signal, with emergent onsets, and an absence
⁶⁸ of clear impulsive phases. Tectonic tremor have been explained as a swarm of

69 small, low-frequency earthquakes (LFEs) (Shelly et al., 2007), which are small
70 magnitude earthquakes ($M \sim 1$) whose frequency content (1-10 Hz) is lower than
71 for ordinary earthquakes (up to 20 Hz). In subduction zones such as Nankai
72 and Cascadia, tectonic tremor observations agree spatially and temporally with
73 slow slip observations (Rogers and Dragert, 2003; Obara et al., 2004). Due to
74 this agreement, these paired phenomena have been called Episodic Tremor and
75 Slip (ETS). However, this is not always the case. For instance, in northern New
76 Zealand, tremor is more challenging to detect, and seems to be located downdip
77 of the slow slip on the plate boundary (Todd and Schwartz, 2016). In Alaska,
78 the tremor zone only partially overlaps the long-term slow slip zone and there
79 does not appear to be any temporal agreement between tremor and slow slip
80 occurrence (Wech, 2016).

81

82 In Cascadia, there are robust signals in both slow slip and tremor (Hawthorne
83 and Rubin, 2013). This is also the case in Nankai (Hiramatsu et al., 2008),
84 where tiltmeters are used instead of GNSS. It is thus possible to use tremor as
85 a proxy to observe slow slip events that are not directly observed in the GNSS
86 data. For instance, Aguiar et al. (2009) studied 23 ETS events in Cascadia
87 with more than 50 hours of tectonic tremor. For all these events, they com-
88 puted both the GPS-estimated moment release and the cumulative number of
89 hours of tectonic tremor recorded. They observed a linear relationship between
90 moment release and number of hours of tremor for slow slip events of moment
91 magnitude 6.3 to 6.8. Based on this linear relationship, it is possible to infer
92 the existence of smaller slow slip events of magnitude 5-6 occurring simultane-
93 ously with smaller tremor bursts of duration 1 to 50 hours occurring in between
94 the big ETS events, and for which there is no detectable signal in the GPS data.

95

96 Frank (2016) divided GPS time series observations from Cascadia and Guer-
97 rero, Mexico, into two groups: the first group contains days with abundant
98 tremor and LFEs, the second group contains days when the number of tremor
99 or LFEs is lower than a threshold. He then stacked separately the two groups
100 of daily observations and observed a cumulative displacement in the direction
101 corresponding to the loading period when few tremor or LFEs are observed
102 and the surface deformation corresponds to the secular plate motion. He also
103 observed a cumulative displacement in the opposite direction corresponding to
104 the release period when tremor and LFEs are observed. He was thus able to
105 observe a reverse displacement corresponding to smaller slow slip events not
106 directly observable in the GPS data for individual events.

107

108 However, these methods cannot be applied to detect slow slip events in places
109 where tremor and slow slip occurrence are not well spatially and temporally cor-
110 related, tremor is not abundant, or the seismic network is not robust enough.
111 We thus need other methods to be able to better detect and quantify slow slip.

112

113 Wavelet methods such as the Discrete Wavelet Transform (DWT) are math-
114 ematical tools for analyzing time series simultaneously in the time and the fre-
115 quency domain by observing how weighted differences of a time series vary from
116 one period to the next. Wavelet methods have been widely used for geophysical
117 applications (e.g. Kumar and Foufoula-Georgiou (1997)). However, few studies
118 have used wavelet methods to analyze recordings of slow slip, and their scope
119 was limited to the detection of the bigger (magnitude 6-7) short-term (a few
120 weeks) events (Szeliga et al., 2008; Ohtani et al., 2010; Wei et al., 2012; Alba
121 et al., 2019).

122

123 Szeliga et al. (2008) determined the timing and the amplitude of 34 slow
124 slip events throughout the Cascadia subduction zone between 1997 and 2005
125 using wavelets. They modeled the GPS time series by the sum of a linear trend,
126 annual and biannual sinusoids representing seasonal effects, Heaviside step func-
127 tions corresponding to earthquakes and hardware upgrades, and a residual sig-
128 nal. They then applied a Gaussian wavelet transform to the residual time series
129 to get the exact timing of slow slip at each GPS station. The idea is that the
130 wavelet transform allows us to analyze the signal both in the time and the fre-
131 quency domains. A sharp change in the signal will be localized and seen at all
132 time scales of the wavelet decomposition, contrary to what happens with the
133 periodic sinusoids of the Fourier transform.

134

135 Instead of using wavelets in the time domain, Ohtani et al. (2010) used 2D
136 wavelet functions in the spatial domain to detect slow slip events. They de-
137 signed the Network Stain Filter (NSF) to detect transient deformation signals
138 from large-scale geodetic arrays. They modeled the position of the GPS station
139 by the sum of the secular velocity, a spatially coherent field, site-specific noise,
140 reference frame errors, and observation errors. The spatial displacement field is
141 modeled by the sum of basis wavelets with time-varying weights. Their method
142 has been successfully used to detect a transient event in the Boso peninsula,
143 Japan, and a slow slip event in the Alaska subduction zone (Wei et al., 2012).

144

145 Finally, Alba et al. (2019) used hourly water level records from four tide
146 gauges in the Juan de Fuca Straight and the Puget Sound to determine relative
147 vertical displacements associated with slow slip events between 1996 and 2011.
148 Their main idea is that the tidal level measured at a given gauge is the sum of
149 a noise component at multiple timescales (tides, ocean and atmospheric noise)

150 and an uplift signal due to the slow slip events. The noise component is assumed
151 to be coherent between all tidal gauges, while the tectonic uplift signal is differ-
152 ent provided that the gauges are far enough from each other. By stacking the
153 tidal records after removing tides, the uplift signals cancel each other while the
154 noise signal is amplified. By stacking the components at different time scales of
155 the DWT decomposition, instead of stacking the raw tidal record, each of the
156 components of the noise at different time scales is retrieved and can then be
157 removed from the raw records to obtain the uplift signal. Due to the relative
158 location of the tidal gauges at Port Angeles and Port Townsend compared to the
159 slow slip region on the plate boundary, a slow slip event should result in uplift
160 in Port Angeles (western part) and in subsidence in Port Townsend (eastern
161 part). Indeed, the authors were able to clearly see a difference in the sign of the
162 uplift at these two tidal gauges.

163

164 In our study, we use a similar approach to previous studies with a different
165 reasoning. We only stack signals at nearby GPS stations, assuming that the
166 east-west displacement due to the slow slip events will then be the same at each
167 of the GPS stations considered. We suppose that some of the noise component
168 is different at each GPS station and will be eliminated by the stacking. Finally,
169 we assume that the noise and the longitudinal displacement due to the slow
170 slip events and the secular plate motion have different time scales, so that the
171 wavelet decomposition will act as a bandpass filter to retrieve the displacement
172 signal and highlight the slow slip events. We use wavelet methods to analyze
173 GPS and tremor recordings of slow slip events in Cascadia. Our objective is
174 to verify that there is a good agreement between slow slip events detected with
175 only GNSS data, and slow slip events detected with only tremor data. We thus
176 want to demonstrate that the wavelet-based detection method can be applied to

177 detect slow slip events that may currently be obscured using standard methods.
178 Finally, we apply the method to GNSS data in New Zealand and successfully
179 detect several slow slip events without needing to rely on the tremor data.

180

181 2 Data

182 We first focused our study on northwest Washington State. For the GNSS data,
183 we used the GPS time series provided by the Pacific Northwest Geodetic Ar-
184 array, Central Washington University. These are network solutions in ITRF2014
185 with phase ambiguities resolved with wide-lane phase-biases. Orbit and satel-
186 lite clocks provided by the Jet Propulsion Laboratory/NASA. North, East, and
187 Vertical directions are available. However, as the direction of the secular plate
188 motion is close to the East direction, we only used the East direction of the GPS
189 time series for the data analysis, as it has the best signal-to-noise ratio. The
190 wavelet method works best with data with zero mean, and no sharp discontinu-
191 ities; so we use the cleaned dataset, that is GPS times series with linear trends,
192 steps due to earthquakes or hardware upgrades, and annual and semi-annual
193 sinusoids signals simultaneously estimated and removed following Szeliga et al.
194 (2004). For the tremor data, we used the tremor catalog from the Pacific North-
195 west Seismic Network (PNSN) (Wech, 2010).

196

197 For the application to slow slip events in New Zealand, we used the GPS
198 time series provided by the Geological hazard information for New Zealand
199 (GeoNet). The coordinates have been extracted by GeoNet during the GLOBK
200 run from the combined daily solution files, and converted to (east, north, up)
201 displacement in millimeters with respect to an a priori position and epoch in the
202 ITRF2008 realization. The time series provided by GeoNet have no adjustments

203 made to them, so they may, for example, contain offsets due to earthquakes,
204 offsets due to equipment changes at individual sites, and seasonal (annual and
205 semi-annual) signals due to various causes. Here again, the direction of the
206 secular interseismic plate motion is close to the West direction, so we only used
207 the East-West component of the GPS time series for the data analysis. We
208 detrended the data before applying the wavelet transform by carrying a linear
209 regression of the whole time series and removing the straight line obtained from
210 the regression.

211 3 Method

212 3.1 The Maximal Overlap Discrete Wavelet Transform

213 The Discrete Wavelet Transform (DWT) is an orthonormal transform that
214 transforms a time series X_t ($t = 0, \dots, N - 1$) into a vector of wavelet coeffi-
215 cients W_i ($i = 0, \dots, N - 1$). If we denote J the level of the wavelet decom-
216 position, and the number of observations is equal to $N = n * 2^J$, where n is
217 some integer greater than or equal to 1, the vector of wavelet coefficients can be
218 decomposed into J wavelet vectors W_j of lengths $\frac{N}{2}, \frac{N}{4}, \dots, \frac{N}{2^J}$, and one scaling
219 vector V_J of length $\frac{N}{2^J}$. Each wavelet vector W_j is associated with changes on
220 time scale $\tau_j = dt2^{j-1}$, where dt is the time step of the time series, and cor-
221 responds to the filtering of the original time series with a filter with nominal
222 frequency interval $[\frac{1}{dt2^{j+1}}; \frac{1}{dt2^j}]$. The scaling vector V_J is associated with aver-
223 ages in time scale $\lambda_J = dt2^J$, and corresponds to the filtering of the original
224 time series with a filter with nominal frequency interval $[0; \frac{1}{dt2^{j+1}}]$. Wavelet vec-
225 tors can be further decomposed into details and smooths, which are more easily
226 interpretable. We define for $j = 1, \dots, J$ the j th wavelet detail D_j , which is a
227 vector of length N , and is associated to time scale $\tau_j = dt2^{j-1}$. Similarly, we can

228 define for $j = 1, \dots, J$ the j th wavelet smooth S_j , which is a vector of length
 229 N , and is associated to scales $\tau_{j+1} = dt2^{j+1}$ and higher. The basic idea is to
 230 reapply to W_j the wavelet filter that was used to construct W_j from the initial
 231 time series X . Together, the details and the smooths define the multiresolution
 232 analysis (MRA) of X :

$$233 \quad X = \sum_{j=1}^J D_j + S_J \quad (1)$$

234 The DWT presents several disadvantages. First, the length of the time se-
 235 ries must be a multiple of 2^J where J is the level of the DWT decompositon.
 236 Second, the time step of the wavelet vector W_j is $dt2^j$, which may not corre-
 237 spond to the time when some interesting phenomenon is visible on the original
 238 time series. Third, when we circularly shift the time series, the corresponding
 239 wavelet coefficients, details and smooths are not a circularly shifted version of
 240 the wavelet coefficients, details and smooths of the original time series. Thus,
 241 the values of the wavelet coefficients, details and smooths are strongly dependent
 242 on the time when we start experimentally gathering the data. Finally, when we
 243 filter the time series to obtain the details D_j and smooths S_j , we introduce a
 244 phase shift, which makes it difficult to line up meaningfully the features of the
 245 MRA with the original time series.

246
 247 To overcome the disadvantages described above, we use instead the Maxi-
 248 mal Overlap Discrete Wavelet Transform (MODWT). The MODWT transforms
 249 the time series X_t ($t = 0, \dots, N - 1$) into J wavelet vectors \tilde{W}_j ($j = 1, \dots, J$) of
 250 length N and a scaling vector \tilde{V}_J of length N . As is the case for the DWT,
 251 each wavelet vector \tilde{W}_j is associated with changes on scale $\tau_j = dt2^{j-1}$, and
 252 corresponds to the filtering of the original time series with a filter with nominal
 253 frequency interval $[\frac{1}{dt2^{j+1}}, \frac{1}{dt2^j}]$. The scaling vector \tilde{V}_J is associated with aver-

254 ages in scale $\lambda_J = dt2^J$, and corresponds to the filtering of the original time
 255 series with a filter with nominal frequency interval $[0; \frac{1}{dt2^{J+1}}]$. As is the case for
 256 the DWT, we can write the MRA:

$$257 \quad X = \sum_{j=1}^J \tilde{D}_j + \tilde{S}_J \quad (2)$$

258 The MODWT of a time series can be defined for any length N . The time
 259 step of the wavelet vectors \tilde{W}_j and the scaling vector \tilde{V}_J is equal to the time
 260 step of the original time series. When we circularly shift the time series, the
 261 corresponding wavelet vectors, scaling vector, details and smooths are shifted
 262 by the same amount. The details and smooths are associated with a zero phase
 263 filter, making it easy to line up meaningfully the features of the MRA with the
 264 original time series. The wavelet methods for time series analysis are explained
 265 in a more detailed way in (Percival and Walden, 2000)).

266

267 The boundary conditions at the two edges of the time series will affect the
 268 wavelet coefficients. For the MODWT, if we denote L the length of the base
 269 wavelet filter used for the wavelet decomposition (in our study, we used a Least
 270 Asymmetric wavelet filter of length $L = 8$, see (Percival and Walden, 2000),
 271 section 4.8, page 107), the length of the wavelet filter at level j used to compute
 272 the wavelet detail D_j is:

$$L_j = (2^j - 1)(L - 1) + 1$$

273 The wavelet coefficients of the detail al level j affected by the boundary con-
 274 ditions at the edges would then be the coefficients with indices $t = 0, \dots, L_j - 2$
 275 or $t = N - L_j + 1, \dots, N - 1$ (see (Percival and Walden, 2000), section 5.11,
 276 page 199). We get $L_j = 442$ for $j = 6$, $L_j = 890$ for $j = 7$ and $L_j = 1786$

277 for $j = 8$. In practice, the part of the wavelet details affected by the boundary
278 conditions is much shorter than that. We compared the wavelet details com-
279 puted when using only the data between 2008 and 2012 and the wavelet details
280 computed when using the entire time series from 2000 to 2021 (Figure S1 in the
281 Supplementary Material). Even at level 8 only about 6 months of data on each
282 side are effected by the boundary conditions.

283 3.2 Application to synthetic data

284 To illustrate the wavelet transform method, we first apply the MODWT to syn-
285 thetic data. As slow slip events occur in Cascadia on a regular basis, every
286 twelve to eighteen months, we create a synthetic signal of period $T = 500$ days.
287 To reproduce the ground displacement observed on the longitudinal component
288 of GPS stations in Cascadia, we divide each period into two parts: In the first
289 part of duration $T - N$, the displacement is linearly increasing and corresponds
290 to the inter seismic plate motion in the eastern direction; in the second part
291 of duration N , the displacement is linearly decreasing and corresponds to a
292 slow slip event on a reverse fault at depth triggering a ground displacement in
293 the western direction. To see the effect of the duration of the slow slip event,
294 we use different values for $N = 5, 10, 20, 40$ days. The amplitude of the set is
295 normalized to 1. Figure 1 shows the synthetics, the details D_j of the wavelet
296 decomposition for levels 1 to 10, and the smooth S_{10} for the four durations of a
297 slow slip event.

298
299 The ramp-like signal is transformed through the wavelet filtering into a wave-
300 form with first a positive peak and then a negative peak. The shape of the wave-
301 form is the same for every level of the wavelet decomposition, but the width of
302 the waveform increases with the scale level. For the 8th level of the wavelet de-

303 composition, the width of the waveform is nearly as large as the time between
304 two events. At larger scales, the waveforms start to merge two contiguous events
305 together, and make the wavelet decomposition less interpretable. For an event
306 of duration 5 days, the wavelet details at levels higher than 3 have a larger
307 amplitude than the wavelet details at lower scales. For an event of duration 10
308 days, the wavelet details at levels higher than 4 have a larger amplitude than
309 the wavelet details at lower scales. For an event of duration 20 days, the wavelet
310 details at levels higher than 5 have a larger amplitude than the wavelet details
311 at lower scales. For an event of duration 40 days, the wavelet details at levels
312 higher than 6 have a larger amplitude than the wavelet details at lower scales.
313 Thus, the scale levels at which an event is being seen in the wavelet details give
314 us an indication about the duration (and the magnitude) of the slow slip event.
315 The big slow slip events of magnitude 6-7 typically trigger a signal that lasts
316 about one week at an individual GPS station, and the whole event lasts several
317 weeks. We expect them to start being visible at the level 5 of the wavelet de-
318 composition, but to not be noticeable at lower time scales.

319

320 3.3 MODWT of GPS and tremor data

321 The DWT and MODWT methods must be used on a continuous time series,
322 without gaps in the recordings. To deal with the gaps in the GNSS recordings,
323 we simply replace the missing values by interpolation. The value for the first
324 day for which data are missing is equal to the mean of the five days before
325 the gap. The value for the last day for which data are missing is equal to the
326 mean of the five days after the gap. The remaining missing values are com-
327 puted by doing a linear interpolation of the first and the last values and adding
328 a Gaussian noise component with mean zero and standard deviation equal to

329 the standard deviation of the whole time series. We verify how the wavelet
330 details may be affected by looking at a GPS time series without missing values
331 and compared the wavelet details with and without removing some data points.
332 Station PGC5 recorded continuous 1390 days between 2009 and 2013 without
333 any missing values. We first computed the wavelet details without missing val-
334 ues. Then, we removed ten neighboring values, replaced them using the method
335 described above (linear interpolation plus Gaussian noise), and computed the
336 wavelet details with the replaced values. Figure S2 in the Supplementary Ma-
337 terial shows a comparison of the two wavelet details for two different locations
338 of the missing values. We can see that there are visible differences in the time
339 series itself, and in the details at the smallest levels of the wavelet decompo-
340 sition. However, the differences between the wavelet details with and without
341 missing values get smaller and smaller with increasing levels of details, and are
342 barely visible for the levels that are most relevant (levels 6 and above). We thus
343 conclude that we can easily replace the missing values in the GNSS time series
344 without introducing false detections of slow slip events.

345

346 We then applied the wavelet filtering to real GPS data. Figure 2 shows the
347 longitudinal displacement for GPS station PGC5, located in southern Vancou-
348 ver Island, the details of the wavelet decomposition for levels 1 to 8, and the
349 smooth. In the data, we can see a sharp drop in displacement whenever there is
350 a documented slow slip event. For levels 5 to 8, which correspond to time scales
351 16, 32, 64 and 128 days, we can see in the details a positive peak followed by
352 a negative peak whenever there is a drop in displacement in the data. We thus
353 verify that the wavelet method can detect steps in the time series associated
354 with slow slip events.

355

356 To increase the signal-to-noise ratio and better detect slow slip events, we
357 stack the signal from several neighboring GPS stations. We choose to focus on
358 GPS stations located close enough to the tremor zone to get a sufficiently high
359 amplitude of the slow slip signal. We choose 16 points along the 40 km depth
360 contour of the plate boundary (model from Preston et al. (2003)) with spacing
361 equal 0.1 degree in latitude (red triangles on Figure 3). Then we took all the
362 GPS stations located in a 50 km radius for a given point, compute the wavelet
363 details for the longitudinal displacement of each station, and stack each detail
364 over the GPS stations. We thus have a stacked detail for each level 1 to 10 of
365 the wavelet decomposition.

366

367 To assess the success of the wavelet decomposition for detecting slow slip
368 events in GPS time series, we validate the approach by comparing to an inde-
369 pendent proxy for slow slip events. We took all the tremor epicenters located
370 within a 50 km radius centered on one of the 16 locations marked by red trian-
371 gles on Figure 3. Then we computed the cumulative number of tremor within
372 this circle. Finally, we removed a linear trend from the cumulative tremor count,
373 and applied the wavelet transform. Because of the preprocessing applied to the
374 tremor data before that wavelet transform, the measurement unit associated
375 with the corresponding wavelet details is the fraction of tremor in a day divided
376 by the total number of days. The average value is 1 divided by the total number
377 of days. Figure 4 shows an example of the wavelet decomposition for the third
378 northernmost location on Figure 3 (which is closest to GPS station PGC5).
379 Contrary to what happens for the GPS data, we see a sharp increase in the
380 time series whenever there is a tremor episode, which translates into a negative
381 peak followed by a positive peak in the wavelet details.

382 **4 Application to data from Cascadia**

383 We stacked the 8th level detail of the wavelet decomposition of the displacement
384 over all the GPS stations located in a 50 km radius of a given point, for the 16
385 locations indicated in Figure 3. The result is shown in the top panel of Figure 5,
386 where each line represents one of the locations along strike. To better highlight
387 the peaks in the wavelet details, we highlighted in red the time intervals where
388 the amplitude of the stacked detail is higher than a threshold, and in blue the
389 time intervals where the amplitude of the stacked detail is lower than minus the
390 threshold. To compare the GPS signal with the tremor signal, we plotted the
391 8th level detail of the wavelet decomposition of the tremor count on the bottom
392 panel of Figure 5. We multiplied by -1 the cumulative tremor count for the
393 wavelet decomposition in order to be able to match positive peaks with positive
394 peaks and negative peaks with negative peaks. In the tremor catalog from the
395 PNSN, there are 17 tremor events with more than 150 hours of tremor recorded.
396 The events are summarized in Table 1. The time of the event is the start date
397 plus half the duration of the event.

398

399 Although the latitudinal extension of the events is not always the same for
400 the GPS data and for the tremor data, we identify the same 13 events in both 8th
401 wavelet decompositions for the 8th level: January 2007, May 2008, May 2009,
402 August 2010, August 2011, September 2012, September 2013, August-November
403 2014, January 2016, March 2017, June 2018, March-November 2019, and Oc-
404 tober 2020-January 2021. Although there are two events in the tremor catalog
405 in August 2014 and November 2014, these two events are not distinguishable in
406 the 8th level details and look more like a single event slowly propagating from
407 South to North. The same phenomenon is observed in 2019 when two tremor
408 events in March and November 2019 are merged into a single event propagating

409 slowly from South to North. In 2020-2021, the wavelet decomposition of the
410 tremor shows one event in the south in October-November 2020 and one event
411 in the North in January 2021, but in the wavelet decomposition of the GPS
412 data, these three events look like a single event propagating slowly from South
413 to North.

414

415 A similar comparison is shown for the wavelet decomposition of the GPS
416 data and the wavelet decomposition of the tremor count data for the 7th level
417 and the 6th level respectively (Figures 6 and 7). The events are harder to see in
418 the 7th level than in the 8th level, both for the GPS data and the tremor count
419 data. The wavelet decomposition is more noisy for the GPS data between 2010
420 and 2012, but it does not seem that there are more slow slip events visible in
421 the 7th level.

422

423 For the 6th level detail, we see an additional event in the South in Fall 2009
424 that is present both in the GPS and the tremor data. It may correspond to the
425 northern extent of a big ETS event occurring in Fall 2009 south of the study
426 area (event 19 in the Michel et al. (2019) catalog). There are three small sig-
427 nals in the GPS data in Winter 2012, Fall 2017, and Winter 2020 that are not
428 present in the tremor data, and may be false detections. To summarize, we
429 assume that robust detections are events present in both GPS and tremor time
430 series, and false detections are events present in the GPS but not in the tremor
431 time series. Then, all the 13 events present on the 8th level detail of the wavelet
432 decomposition are robust detections and 14 of the 17 events present on the 6th
433 level detail of the wavelet decomposition are robust detections.

434

435 To better evaluate the number of robust and false detections, we convert

436 the wavelet details into trinary time series. If the absolute value of the wavelet
 437 detail is higher than a threshold, we replace the value by 1 (for positive values)
 438 or -1 (for negative values), otherwise we replace the value by 0. We do this
 439 on both the wavelet details of the GPS data and of the tremor data. Then we
 440 decide that if both the GPS and the tremor time series take the value 1 (or
 441 both take the value -1), we have a robust detection (true positive, TP). If the
 442 GPS and the tremor time series have opposite signs, or if the absolute value of
 443 the GPS time series is 1 but the value of the tremor time series is 0, we have a
 444 false detection (false positive, FP). If both time series take the value 0, we do
 445 not have detection (true negative, TN). If the GPS time series take the value
 446 0, but the absolute value of the tremor time series is 1, we miss a detection
 447 (false negative, FN). We then define the sensitivity (true positive rate) and the
 448 specificity (equal to 1 minus the false positive rate) as:

$$\begin{aligned}
 \text{sensitivity} &= \frac{TP}{TP + FN} \\
 \text{specificity} &= \frac{TN}{TN + FP}
 \end{aligned} \tag{3}$$

449 We can then evaluate the quality of the detections obtained with our method
 450 by plotting a receiver operating characteristic curve (ROC curve). The ROC
 451 curve is widely used for binary classification problems in statistics and machine
 452 learning. We calculate an ROC value by varying the values of the threshold
 453 (here the two thresholds used to convert the GPS and the tremor time series
 454 into trinary time series), computing the corresponding values of the true positive
 455 rate and the false positive rate (equal to 1 minus the specificity), and plotting
 456 the true positive rate as a function of the false positive rate. If the classifica-
 457 tion was made randomly, all the points would fall on the first diagonal. If the
 458 classifier was perfect, the corresponding point would fall on the top left cor-
 459 ner of the graph with true positive rate equal to 1 and false positive rate equal

460 to 0. The bigger the area under the curve, the better the classification method is.

461

462 As the slow slip events are better seen on levels 6, 7 and 8 of the wavelet
463 decomposition, we first add the wavelet details corresponding to levels 6 to 8,
464 and transform the resulting time series into a trinary time series. We apply this
465 transform to both the GPS and the tremor time series with varying thresholds.
466 We then plot the ROC curve on Figure 8, each dot representing a different
467 threshold. The corresponding sums of the wavelet details for the GPS data and
468 the tremor data are shown on Figure 9. We can see that there is a trade-off
469 between sensitivity and specificity as we vary the threshold. If we decrease the
470 false positive rate, we also decrease the number of true events detected. If we
471 increase the number of true events detected, we also increase the false positive
472 rate. If we increase the threshold for the tremor, the curve goes farther away
473 from the first diagonal, that is we get better classification results. If we increase
474 the threshold for the GPS, the false positive rate and the the number of events
475 detected decrease. In Figure 9, we have chosen thresholds for the GPS time
476 series and the tremor time series such that the specificity is higher than 0.75
477 (that is the false positive rate is lower than 0.25), and the sensitivity is the
478 highest possible, that is we have chosen the thresholds corresponding to the dot
479 that is farthest from the diagonal, which is random.

480

481 In addition to the magnitude 6 events discussed above, Michel et al. (2019)
482 have also identified several magnitude 5 events using a variational Bayesian In-
483 dependent Component Analysis (vbICA) decomposition of the signal. As we
484 expect smaller magnitude events to be more visible at smaller time scales of the
485 wavelet decomposition (level 5), we verify for all these events whether a signal
486 can be seen at the same time as the time given in their catalog. Most of these

487 magnitude 5 events are also sub-events of bigger magnitude 6 events. Table
488 2 summarizes for each event its timing, its number and its magnitude as indi-
489 cated in the catalog from Michel et al. (2019), and whether it is part of a bigger
490 magnitude 6 event. Figure 10 shows the 5th level detail wavelet decomposition
491 of the GPS data. Red lines show the timing of the big slow slip events from
492 Table 1, and blue lines show the timing of the small slow slip events from Table 2.

493

494 All 14 events that are sub-events of a bigger event are visible at level 5.
495 However, this may be because the bigger events are clearly seen at levels 6 to 8,
496 and also at smaller time scales. The one small event that is not part of a bigger
497 event (Winter 2009) is visible at level 5 of the wavelet decomposition. However,
498 some other events that are not in the catalog of Michel et al. (2019)'s catalog
499 are also visible in late 2007, early 2010, early 2012, and early 2020. Therefore,
500 it is difficult to differentiate between a robust detection and a false detection,
501 and to conclude whether the method can indeed detect events of magnitude 5.

502

503 In Figure 9, we see four smaller events that are not in the catalog of Michel
504 et al. (2019): at about 2007.5, there is a negative peak followed by a positive
505 peak (that is an event in the opposite direction of what would be expected from
506 slow slip), at about 2010.2, 2012.2 and 2020.2, there are positive peaks followed
507 by negative peaks for all the sixteen locations studied in this paper. These
508 events are highlighted in Figure S4 in the Supplementary Information. Looking
509 back at the original GPS data, there is a small increase in the displacement
510 in the eastern direction that lasts about one or two months at about 2007.5.
511 However, the direction of the displacement does not correspond to a slow slip
512 event, and another cause should be found to explain this signal. There is a de-
513 crease in displacement that lasts several months at about 2010.2. This transient

514 may correspond to a long duration slow slip event. There is a small decrease
515 in displacement at about 2012.2. Its amplitude is small but the duration and
516 direction correspond to a slow slip event, so this transient could be a very small
517 slow slip event. Finally, there is also a small decrease in displacement at about
518 2020.2 that is difficult to interpret.

519

520 Due to the short distances between the GPS stations and the locations of the
521 red triangles on the map from Figure 3, the same station could be used multiple
522 times for the stacking at different locations. When considering two different lo-
523 cations, the stacking is thus made over an overlapping number of stations. Table
524 3 summarizes the number of stations and the number of overlapping stations for
525 each location on Figure 3. We hypothesize that the small displacement in the
526 eastern direction seen at about 2007.5 could be due to a misbehaving station
527 common to several locations. However, several GPS stations indeed show an
528 increase in the displacement in the eastern direction at about 2007.5. There are
529 many missing data around that time, so it is difficult to conclude.

530

531 Another possibility is that common mode signals could stack constructively
532 across GNSS stations and produce peaks in the wavelet details that are actually
533 due to non-tectonic signals. We computed common mode signals for different
534 latitude bins (each bin has width equal to half-a-degree of latitude) following
535 the same method as Nuyen and Schmidt (2021). We first stacked all the time
536 series for the stations in each latitude bin that are located more than 100 km
537 east of the 40 km depth contour of the plate boundary. We assume that these
538 stations are not sensitive to the deformation on the plate interface. We then
539 apply a yearly moving average to each common mode signal in order to remove
540 any leftover noise. The common mode signal was then removed from the GNSS

541 time series depending on each sites latitude. Figure S3 in the Supplementary
542 Information shows the corresponding sum of the stacks of the 6th, 7th and 8th
543 wavelet details obtained from the resulting time series. The common modes
544 seem to have little impact on the results and do not explain the additional four
545 small events that we noted in Figure 9.

546

547 In order to convert our filtered eastward displacement time series into a slow
548 slip event catalog we note that red bars represent displacements exceeding a
549 threshold of 0.8 mm (east), and blue marks displacements less than minus -0.8
550 mm (west). During times with no slow slip GPS stations on the overriding plate
551 are pushed slowly eastward by the locked subducting plate. Slow slip events
552 represent GPS motion towards the west. Thus, we infer that slow slip events
553 happen when red bars are immediately followed by blue bars in the wavelet
554 details. We have identified everywhere that this has happened and mark it with
555 a green line in Figure 11 and as a row in Table 4. We find 17 possible SSEs
556 by this method using filtered GPS data only. For each of these 17 events we
557 determine the time difference between the mid time of the GPS catalog and the
558 nearest time from the tremor catalog (Table 1). These time differences are in
559 column 6 (Table 4). Every event in the GPS catalog has a match in the tremor
560 catalog except for the tremor event at 2010.15. There is also only one event in
561 the tremor catalog that is not in the GPS catalog. It occurs at 2014.65 with
562 a duration of 15 days and 190 hours of tremor. It occurs 0.25 years after the
563 nearest GPS event. There are also two marginal events in the tremor catalog
564 with time differences of 0.13 and 0.10 years, but those are also among the smaller
565 events with 162 and 193 hours of tremor.

566 **5 Application to data from New Zealand**

567 We now apply our wavelet-based method to detect slow slip events in New
568 Zealand, a location where the spatial and temporal agreement between tremor
569 and slow slip is not as good as in other subduction zones. The tectonics of
570 the North Island of New Zealand are dominated by the westward subduction
571 of the Pacific Plate under the Australian Plate at the Hikurangi Trench. Two
572 types of slow slip events have been observed at the Hikurangi margin. Shallow
573 (10-15 km depth), shorter (1-3 weeks), and usually smaller (Mw 6.3-6.8) slow
574 slip events have been observed every 18-24 months in the northern part of the
575 margin. Deeper (35-60 km depth), longer (12-18 months), and larger (Mw 7.0)
576 slow slip events have been observed every 5 years in the southern part of the
577 margin (Wallace and Beavan, 2010; Todd and Schwartz, 2016). The detection of
578 tremor has been elusive in northern Hikurangi. Delahaye et al. (2009) observed
579 an increase in the rate of microseismicity downdip of the 2004 Gisborne slow slip
580 event. More recently, however, (Kim et al., 2011) detected a low level of tremor
581 activity that increased during the 2010 Gisborne slow slip event. As was the
582 case for the microearthquakes, the source of the tremor was located downdip of
583 the slow slip patch determined from GNSS data. (Ide, 2012) detected tremor
584 downdip of the location of two deep slow slip events observed by Wallace and
585 Eberhart-Phillips (2013) in 2006 and 2008. However, contrary to ETS events
586 in Cascadia and Nankai, the tremor activity did not seem to increase during
587 the slow slip events. Todd and Schwartz (2016) detected tremor associated
588 with most of the shallow slow slip events between 2010 and 2015, and located
589 downdip of the geodetically inferred slip area. They also detected deeper tremor
590 between 20 and 50 km depth with unclear origin. They hypothesized that these
591 tremor may be related to undetected deep long-term slow slip events.

592

593 To evaluate whether the wavelet analysis is effective in a region without
594 robust tremor, we take all the New Zealand GPS stations located in a 50 km
595 radius of a given location, for the 18 locations indicated in Figure 12, and we
596 stack the 6th level details, the 7th level details or the 8th level details over all
597 the GPS stations. We then sum together the 6th, 7th and 8th levels stacked
598 wavelet details (Figure 13, top panel). We highlight positive and negative peaks
599 with red and blue colors as was done in Figure 9. We cannot use the tremor
600 data to decide what is the appropriate threshold above which we consider that
601 there is a slow slip event. Slow slip events in New Zealand result in surface dis-
602 placements that are similar in amplitude to twice as large as those observed in
603 Cascadia. Therefore, the amplitudes of the peaks in the wavelet details should
604 be similar in New Zealand and in Cascadia and we choose identical thresholds
605 for both regions. As a slow slip event in northern New Zealand results in a
606 displacement in the east direction at the earths surface, the slow slip events are
607 indicated by a negative peak followed by a positive peak in the stacked wavelet
608 details. We compare the results of the timings and locations of the slow slip
609 events to those events detected by Todd and Schwartz (2016). As they only
610 used data from five GPS stations (PUKE, ANAU, GISB, MAHI and CKID),
611 we indicate by a vertical orange bar on the bottom panel of Figure 13 each time
612 a slow slip event was detected for these stations. The orange bars are centered
613 on the latitudes of the GPS stations. If a slow slip event was detected by more
614 than one station, all the corresponding orange bars are linked together to show
615 the spatial extent of the slow slip. Todd and Schwartz (2016) indicated by a
616 question mark (on their Figure 2 and their Table 1) additional possible events,
617 and those are indicated by a dotted orange bar on Figure 13. To compare with
618 the slow slip events detected with the wavelet method, we also mark by a green
619 bar every time a negative peak lower than the threshold is followed by a pos-

620 itive peak higher than the threshold. Table 5 summarizes the slow slip events
621 detected with the wavelet method for 2010-2016.

622

623 We observe that there is a good agreement between the events detected
624 with the wavelet method and the events previously detected by Todd and
625 Schwartz (2016). We clearly see an event propagating from south to north
626 in January-February (event 2 from Todd and Schwartz (2016)), an event in
627 March-April 2010 (event 3), an event in April-May 2011 in the northern part
628 of the region studied (events 6 and 7), an event propagating south-to-north in
629 August-September and September-October 2011 (events 8 and 9), and an event
630 in December 2011 (event 10). Although Todd and Schwartz (2016) only de-
631 tected this last event for GPS station GISB, it seems that this event may have
632 also extended farther to the north and the south. We then clearly see an event
633 in the northern part of the region studied in August 2012 (event 12), an event
634 in December 2012-January 2013 (event 13), an event in the southern part of
635 the region studied in February-March 2013 (event 14), an event propagating
636 from south to north in June-July and July-August 2013 (events 15 and 16), an
637 event in September 2014 (events 20 and 21), an event in the southern part of
638 the region studied in December 2014-January 2015 (events 22 and 23), and an
639 event in June-July 2015 in the northern part of the region studied (event 26).
640 It is unclear if the event near station ANAU in early 2010 (event 1) is visible
641 in the wavelet details as it is too close to the beginning of the time series. The
642 June-July 2010 event (event 4), the August 2010 event (event 5), and the March
643 2012 event (event 11), are not clearly visible in the wavelet details. The events
644 in September-October 2013 (event 17), December 2013 (event 18), May-June
645 2014 (event 19), January-February (event 24) and February 2015 (events 25)
646 are not clearly seen in the wavelet details, but there could be a small negative

647 peak followed by a small positive peak at these times. Additionally, there could
648 be two other events that are not in (Todd and Schwartz, 2016) in Fall 2010
649 (southern part of the region studied) and in Fall 2015.

650

651 Our wavelet-based method thus works well to detect transients in GPS data
652 that could be slow slip events, even in the absence of tremor data. The choice
653 of the appropriate threshold to decide that there is a transient and the levels
654 of the wavelet details that we look at for the detection may still not be easily
655 made. There is a difference between Cascadia and New Zealand in terms of
656 which wavelet details to stack. In particular, as there is more time between
657 two slow slip events in New Zealand than in Cascadia, the biggest slow slip
658 events (early 2010, late 2011, 2013 and late 2014) can also be seen on the 9th
659 level detail for New Zealand, whereas they could not be seen for Cascadia. We
660 then use the method to detect slow slip events during the period 2016-2022,
661 which was not covered by Todd and Schwartz (2016) (Figure 14). We note
662 four large transients that could be slow slip events in late 2016, late 2017, early
663 2019 and mid-2021. There are also possible smaller events in the northern part
664 of the area in mid-2018 and in most of the area studied in early 2020. Table 6
665 summarizes the slow slip events detected with the wavelet method for 2016-2022.

666

667 The method is thus applicable in regions where tremor data are not usable.
668 To determine which wavelet levels to stack, we recommend analyzing each level
669 detail. Look for spatially coherent patterns, wavelet details with energy at
670 similar times and high signal-to-noise ratios. Look for alternating positive and
671 negative peaks that are consistent with the expected direction of slow slip.
672 Consider wavelet details with time scales ranging from the expected duration of
673 slow slip events to the expected recurrence times between slow slip events. For

674 Cascadia and New Zealand this would be weeks to years. Determination of a
675 threshold is subjective. At large thresholds the large slow slip events should be
676 clear. At smaller thresholds there is the possibility of identifying smaller events,
677 but at the risk of false detections.

678 6 Conclusion

679 In this paper, we develop and test a new approach for detecting transient events
680 in GPS time series, such as slow slip events. We used wavelet methods to analyze
681 GNSS time series and tremor recordings of slow slip events in Cascadia, and
682 GNSS time series in New Zealand. We used detrended GNSS data, applied the
683 MODWT transform, and stacked the wavelet details over several nearby GNSS
684 stations. As an independent check on the timing of slow slip events, we also
685 computed the cumulative number of tremor in the vicinity of the GNSS stations,
686 detrended this signal, and applied the MODWT transform. In both time series,
687 we could then see simultaneous waveforms whose timing corresponds to the
688 timing of slow slip events. We assumed that there is a slow slip event whenever
689 the wavelet signal gets above a threshold. We verified that there is a good
690 agreement between slow slip events detected with only GNSS data, and slow
691 slip events detected with only tremor data. The wavelet-based detection method
692 detects all events of magnitude higher than 6 as determined by independent
693 event catalogs (e.g. (Michel et al., 2019)). We detected signals in the GPS data
694 that could be magnitude 5 events, but it is not easy to differentiate between
695 robust detections and false detections. We then applied the method to GNSS
696 data in New Zealand and detected slow slip events consistent with the events
697 previously detected by Todd and Schwartz (2016).

698 **Data and Resources**

699 The GPS recordings used for this analysis can be downloaded from the PANGA
700 website (GPS/GNSS Network and Geodesy Laboratory: Central Washington
701 University, other/seismic network, 1996) <http://www.panga.cwu.edu/> and the
702 Geonet website <https://www.geonet.org.nz/>. The Python scripts used to
703 analyze the data and make the figures can be found on the first author's Github
704 account <https://github.com/ArianeDucellier/slowslip>. Figures 3 and 12
705 were created using GMT (Wessel and Smith, 1991). The Supplementary Ma-
706 terial contains three figures showing the effects of boundary conditions, missing
707 data and common modes, and a figure showing four additional small displace-
708 ments detected in the GPS data.

709 **Acknowledgements**

710 The authors would like to thank two anonymous reviewers and the Associate Ed-
711 itor Jeanne Hardebeck, whose comments greatly helped improve the manuscript.
712 This work was funded by the grant from the National Science Foundation EAR-
713 1358512. A.D. would like to thank Professor Donald Percival for introducing
714 her to wavelet methods during his excellent class on Wavelets: Data Analysis,
715 Algorithms and Theory taught at University of Washington.

716 **Declaration of Competing Interests**

717 The authors declare no competing interests.

718 **References**

- 719 Aguiar, A., Melbourne, T., and Scrivner, C. Moment release rate of Cascadia
720 tremor constrained by GPS. *J. Geophys. Res.*, 114:B00A05, 2009.
- 721 Alba, S., Weldon, R. J., Livelybrooks, D., and Schmidt, D. A. Cascadia ETS
722 events seen in tidal records (1980–2011). *Bull. Seismol. Soc. Am.*, 109(2):
723 812–821, 2019.
- 724 Audet, P. and Kim, Y. Teleseismic constraints on the geological environment
725 of deep episodic slow earthquakes in subduction zone forearcs: A review.
726 *Tectonophysics*, 670:1–15, 2016.
- 727 Bartlow, N. M. A longterm view of episodic tremor and slip in Cascadia. *Geo-
physical Research Letters*, 43(3):e2019GL085303, 2020.
- 729 Beroza, G. and Ide, S. Slow earthquakes and nonvolcanic tremor. *Annu. Rev.
Earth Planet. Sci.*, 39:271–296, 2011.
- 731 Delahaye, E., Townend, J., Reyners, M., and Rogers, G. Microseismicity but
732 no tremor accompanying slow slip in the Hikurangi subduction zone, New
733 Zealand. *Earth and Planetary Science Letters*, 277:21–28, 2009.
- 734 Frank, W. Slow slip hidden in the noise: The intermittence of tectonic release.
735 *Geophys. Res. Lett.*, 43:10125–10133, 2016.
- 736 GPS/GNSS Network and Geodesy Laboratory: Central Washington University,
737 other/seismic network. Pacific Northwest Geodetic Array (PANGA), 1996.
738 URL <http://www.panga.cwu.edu/>.
- 739 Hall, K., Houston, H., and Schmidt, D. Spatial comparisons of tremor and slow
740 slip as a constraint on fault strength in the northern Cascadia subduction
741 zone. *Geochemistry, Geophysics, Geosystems*, 19(8):2706–2718, 2018.

- 742 Hawthorne, J. C. and Rubin, A. M. Shorttime scale correlation between slow
743 slip and tremor in Cascadia. *Journal of Geophysical Research: Solid Earth*,
744 118:1316–1329, 2013.
- 745 Hiramatsu, Y., Watanabe, T., and Obara, K. Deep lowfrequency tremors as a
746 proxy for slip monitoring at plate interface. *Geophysical Research Letters*, 35:
747 L13304, 2008.
- 748 Ide, S. Variety and spatial heterogeneity of tectonic tremor worldwide. *Journal*
749 *of Geophysical Research*, 117:B03302, 2012.
- 750 Jiang, Y., Wdowinski, S., Dixon, T. H., Hackl, M., Protti, M., and Gonzalez,
751 V. Slow slip events in Costa Rica detected by continuous GPS observations,
752 2002-2011. *Geochemistry, Geophysics, Geosystems*, 13:Q04006, 2012.
- 753 Kim, M., Schwartz, S., and Bannister, S. Nonvolcanic tremor associated with
754 the March 2010 Gisborne slow slip event at the Hikurangi subduction margin,
755 New Zealand. *Geophysical Research Letters*, 38:L14301, 2011.
- 756 Kumar, P. and Foufoula-Georgiou, E. Wavelet analysis for geophysical applica-
757 tions. *Rev. Geophys.*, 35(4):385–412, 1997.
- 758 Li, S., Freymueller, J., and McCaffrey, R. Slow slip events and timedependent
759 variations in locking beneath Lower Cook Inlet of the AlaskaAleutian sub-
760 duction zone. *Journal of Geophysical Research: Solid Earth*, 121:1060–1079,
761 2016.
- 762 Michel, S., Gualandi, A., and Avouac, J.-P. Interseismic coupling and slow slip
763 events on the Cascadia megathrust. *Pure Appl. Geophys.*, 176:3867–3891,
764 2019.
- 765 Nishimura, T., Matsuzawa, T., and Obara, K. Detection of shortterm slow slip

- 766 events along the Nankai Trough, southwest Japan, using GNSS data. *Journal*
767 *of Geophysical Research: Solid Earth*, 118:3112–3125, 2013.
- 768 Nuyen, C. P. and Schmidt, D. A. Filling the gap in Cascadia: The emergence
769 of lowamplitude longterm slow slip. *Geochemistry, Geophysics, Geosystems*,
770 22(3):e2020GC009477, 2021.
- 771 Obara, K., Hirose, H., Yamamizu, F., and Kasahara, K. Episodic slow slip
772 events accompanied by non-volcanic tremors in southwest Japan subduction
773 zone. *Geophysical Research Letters*, 31:L23602, 2004.
- 774 Ohtani, R., McGuire, J., and Segall, P. Network strain filter: A new tool for
775 monitoring and detecting transient deformation signals in GPS arrays. *J.*
776 *Geophys. Res.*, 115:B12418, 2010.
- 777 Percival, D. and Walden, A. *Wavelet Methods for Time Series Analysis*. Cam-
778 bridge Series in Statistical and Probabilistic Mathematics. Cambridge Uni-
779 versity Press, New York, NY, USA, 2000.
- 780 Preston, L., Creager, K., Crosson, R., Brocher, T., and Trehu, A. Intraslab
781 earthquakes: Dehydration of the Cascadia slab. *Science*, 302:1197–1200, 2003.
- 782 Radiguet, M., Cotton, F., Vergnolle, M., Campillo, M., Walpersdorf, A., Cotte,
783 N., and Kostoglodov, V. Slow slip events and strain accumulation in the
784 Guerrero gap, Mexico. *Journal of Geophysical Research: Solid Earth*, 117:
785 B04305, 2012.
- 786 Rogers, G. and Dragert, H. Tremor and slip on the Cascadia subduction zone:
787 The chatter of silent slip. *Science*, 300(5627):1942–1943, 2003.
- 788 Schmidt, D. A. and Gao, H. Source parameters and timedependent slip dis-
789 tributions of slow slip events on the Cascadia subduction zone from 1998 to
790 2008. *Journal of Geophysical Research: Solid Earth*, 115:B00A18, 2010.

- 791 Shelly, D., Beroza, G., and Ide, S. Non-volcanic tremor and low-frequency
792 earthquake swarms. *Nature*, 446:305–307, 2007.
- 793 Szeliga, W., Melbourne, T., Miller, M., and Santillan, V. Southern Cascadia
794 episodic slow earthquakes. *Geophys. Res. Lett.*, 31:L16602, 2004.
- 795 Szeliga, W., Melbourne, T., Santillan, M., and Miller, M. GPS constraints on 34
796 slow slip events within the Cascadia subduction zone, 1997-2005. *J. Geophys.*
797 *Res.*, 113:B04404, 2008.
- 798 Todd, E. and Schwartz, S. Tectonic tremor along the northern Hikurangi Mar-
799 gin, New Zealand, between 2010 and 2015. *J. Geophys. Res. Solid Earth*, 121:
800 8706–8719, 2016.
- 801 Vergnolle, M., Walpersdorf, A., Kostoglodov, V., Tregoning, P., Santiago, J. A.,
802 Cotte, N., and Franco, S. I. Slow slip events in Mexico revised from the
803 processing of 11 year GPS observations. *Journal of Geophysical Research: Solid Earth*,
804 115:B08403, 2010.
- 805 Wallace, L. M. Slow slip events in New Zealand. *Annual Review of Earth and*
806 *Planetary Sciences*, 48:175–203, 2020.
- 807 Wallace, L. M., Beavan, J., Bannister, S., and Williams, C. Simultaneous
808 longterm and shortterm slow slip events at the Hikurangi subduction margin,
809 New Zealand: Implications for processes that control slow slip event occur-
810 rence, duration, and migration. *Journal of Geophysical Research: Solid Earth*,
811 117:B11402, 2012.
- 812 Wallace, L. and Beavan, J. Diverse slow slip behavior at the Hikurangi sub-
813 duction margin, New Zealand. *Journal of Geophysical Research*, 115:B12402,
814 2010.

- 815 Wallace, L. and Eberhart-Phillips, D. Newly observed, deep slow slip events at
816 the central Hikurangi margin, New Zealand: Implications for downdip vari-
817 ability of slow slip and tremor, and relationship to seismic structure. *Geo-*
818 *physical Research Letters*, 40:5393–5398, 2013.
- 819 Wech, A. Interactive tremor monitoring. *Seismol. Res. Lett.*, 81(4):664–669,
820 2010.
- 821 Wech, A. Extending Alaska’s plate boundary; tectonic tremor generated by
822 Yakutat subduction. *Geology*, 44(7):587–590, 2016.
- 823 Wei, M., McGuire, J., and Richardson, E. A slow slip event in the south central
824 Alaska Subduction Zone. *Geophys. Res. Lett.*, 39:L15309, 2012.
- 825 Wessel, P. and Smith, W. H. F. Free software helps map and display data. *EOS*
826 *Trans. AGU*, 72:441, 1991.
- 827 Williams, C. A., Eberhart-Phillips, D., Bannister, S., Barker, D. H., Henrys, S.,
828 Reyners, M., and Sutherland, R. Revised interface geometry for the Hikurangi
829 subduction zone, New Zealand. *Seismological Research Letters*, 84(6):1066–
830 1073, 2013.

⁸³¹ **Addresses**

⁸³² Ariane Ducellier. University of Washington, Department of Earth and Space
⁸³³ Sciences, Box 351310, 4000 15th Avenue NE Seattle, WA 98195-1310.

⁸³⁴

⁸³⁵ Kenneth C. Creager. University of Washington, Department of Earth and
⁸³⁶ Space Sciences, Box 351310, 4000 15th Avenue NE Seattle, WA 98195-1310.

⁸³⁷

⁸³⁸ David A. Schmidt. University of Washington, Department of Earth and
⁸³⁹ Space Sciences, Box 351310, 4000 15th Avenue NE Seattle, WA 98195-1310.

Tables

Table 1: Episodic Tremor and Slip events with $M > 6$ identified by MODWT in both the GPS and the tremor data. The duration and the number of tremor are from the tremor catalog of the PNSN. The event number and the magnitude are from the slow slip catalog of Michel et al. (2019).

Time	Duration (days)	Number of tremor (hours)	Event number	Magnitude
2007.06	28	398	3	6.68
2008.36	25	402	10	6.56
2009.35	24	248	16	6.49
2010.63	29	518	24	6.54
2011.60	37	479	30	6.47
2012.72	37	620	34	6.54
2013.71	27	423	41	6.58
2014.65	15	190	48	6.03
2014.89	38	385	51	6.40
2016.11	43	421	54	6.79
2017.23	19	279	59	6.61
2018.49	22	381		
2019.23	34	195		
2019.88	16	205		
2020.79	26	193		
2020.86	12	162		
2021.09	14	230		

Table 2: Magnitude 5 to 6 events from Michel et al. (2019).

Time	Event number	Magnitude	Sub-event of bigger event
2007.06	1	5.64	Yes
2007.08	2	5.91	Yes
2008.38	11	5.50	Yes
2009.16	14	5.50	No
2009.36	17	5.32	Yes
2010.63	25	5.76	Yes
2011.66	31	5.61	Yes
2011.66	32	5.32	Yes
2012.69	35	5.56	Yes
2013.74	42	5.71	Yes
2014.69	49	5.31	Yes
2014.93	52	5.39	Yes
2016.03	57	5.80	Yes
2017.13	60	5.43	Yes
2017.22	61	5.37	Yes

Table 3: Number of GPS stations used for the stacking for each location on Figure 3 and number of common stations with the location immediately to the north and the location immediately to the south.

Index	Latitude	Number of stations	Common stations (north)	Common stations (south)
0	47.2	15	14	
1	47.3	18	17	14
2	47.4	24	20	17
3	47.5	21	20	20
4	47.6	22	14	20
5	47.7	17	12	14
6	47.8	13	8	12
7	47.9	10	9	8
8	48.0	10	7	9
9	48.1	8	7	7
10	48.2	10	8	7
11	48.3	9	9	8
12	48.4	9	5	9
13	48.5	7	5	5
14	48.6	6	5	5
15	48.7	5		5

Table 4: Cascadia catalog of slow slip events based only on MODWT analysis of GPS time series and inferring that the transition of red followed immediate by blue marks a slow slip event. First four columns are the start and end times and start and end latitudes of the green bars in Figure 11. The fifth column is 1 for robust detection and 2 if not as robust. Column 6 is the time difference in years between the mid times of the GPS catalog and the nearest mid times of the tremor catalog summarized in Table 1.

start time	end time	start latitude	end latitude	dT	tremor catalog
2007.06	2007.10	47.16	48.72	1	0.02
2008.30	2008.40	47.35	48.73	1	0.01
2009.35	2009.44	47.92	48.73	1	0.05
2010.12	2010.15	47.32	48.73	1	0.50 no match
2010.61	2010.64	47.17	48.72	1	0.00
2011.57	2011.61	47.18	48.68	1	0.01
2012.65	2012.65	48.74	47.76	1	0.05
2013.71	2013.75	47.47	48.73	1	0.02
2014.89	2014.90	48.73	47.79	1	0.01
2015.98	2016.09	48.73	47.20	1	0.08
2017.17	2017.24	47.38	48.72	1	0.02
2018.35	2018.36	47.48	47.93	1	0.13 part of same event?
2018.48	2018.50	48.72	48.09	1	0.00
2019.32	2019.34	47.17	47.72	2	0.10
2019.90	2019.91	48.47	48.72	2	0.02
2020.79	2020.83	47.18	48.13	1	0.02 & 0.05
2021.11	2021.12	48.75	48.48	2	0.02

Table 5: New Zealand catalog of slow slip events for 2010-2016 based only on MODWT analysis of GPS time series and inferring that the transition of red followed immediate by blue marks a slow slip event. First four columns are the start and end times and start and end latitudes of the green bars in Figure 13. The fifth column is 1 for robust detection and 2 if not as robust.

start time	end time	start latitude	end latitude	
2010.05	2010.07	-39.67	-39.12	1
2010.19	2010.22	-39.12	-38.07	1
2010.75	2010.76	-39.73	-39.41	1
2011.36	2011.37	-38.22	-38.02	2
2011.71	2011.74	-37.97	-38.41	1
2011.67	2011.71	-39.73	-38.91	1
2011.92	2011.95	-38.84	-38.16	1
2012.63	2012.63	-39.42	-39.62	2
2012.64	2012.66	-38.53	-38.02	1
2012.95	2012.96	-38.32	-37.98	1
2013.15	2013.16	-38.87	-39.72	1
2013.55	2013.57	-38.62	-38.01	1
2013.74	2013.74	-38.77	-38.97	2
2013.92	2013.93	-38.17	-37.98	2
2013.91	2013.95	-39.37	-39.73	1
2014.78	2014.79	-38.03	-39.03	1
2014.96	2015.00	-39.07	-39.72	1
2015.53	2015.53	-39.42	-39.72	1
2015.52	2015.55	-37.97	-38.43	1
2015.78	2015.79	-38.77	-39.37	1

Table 6: New Zealand catalog of slow slip events for 2016-2022 based only on MODWT analysis of GPS time series and inferring that the transition of red followed immediate by blue marks a slow slip event. First four columns are the start and end times and start and end latitudes of the green bars in Figure 13. The fifth column is 1 for robust detection and 2 if not as robust.

start time	end time	start latitude	end latitude	
2016.84	2016.90	-37.96	-39.72	1
2017.10	2017.10	-38.78	-39.00	2
2017.73	2017.78	-37.98	-38.51	1
2018.04	2018.06	-38.58	-39.07	1
2018.63	2018.64	-38.27	-37.97	2
2019.26	2019.33	-37.97	-39.73	1
2020.09	2020.12	-37.97	-38.23	2
2020.34	2020.35	-37.96	-39.72	1
2020.33	2020.33	-37.96	-38.10	2
2020.32	2020.32	-38.62	-38.79	2
2020.36	2020.37	-39.70	-39.35	2
2021.11	2021.11	-39.51	-39.64	2
2021.39	2021.47	-39.72	-38.08	1

841 **Figure captions**

- 842 • Figure 1. Demonstration of a wavelet decomposition for a synthetic dataset.
843 A synthetic time series is created (top row) with steps of period 500 days,
844 and transient durations of 2 days (left), 5 days, 10 days, and 20 days
845 (right). The resulting details and smooths are shown in increasing level.
846 The amplitude of the synthetic time series is normalized to 1, and the
847 details and smooths show the relative amplitude.
- 848 • Figure 2. Top left: East-west displacement recorded at GPS station
849 PGC5. The resulting details and smooth of the wavelet decomposition
850 are shown in increasing level from top to bottom and from left to right.
- 851 • Figure 3. GPS stations used in this study (black triangles). The black
852 line represents the 40 km depth contour of the plate boundary model by
853 Preston et al. (2003). The red triangles are the locations where we stack
854 the GPS data. The small grey dots are all the tremor locations from the
855 PNSN catalog.
- 856 • Figure 4. Details and smooth of the wavelet decomposition of the de-
857 trended cumulative tremor count around the third northernmost red tri-
858 angles on Figure 3 (latitude 48.5).
- 859 • Figure 5. Top: Stacked 8th level details of the wavelet decomposition of
860 the displacement over all the GPS stations located in a 50 km radius of a
861 given point, for the 16 red triangles indicated in Figure 3. Bottom: 8th
862 level detail multiplied by -1 of the cumulative tremor count in a 50 km
863 radius of a given point for the same 16 locations. The black lines represent
864 the timings of the ETS events from Table 1. We mark by a red rectangle
865 every time where the amplitude is higher than a threshold of 0.4 mm (for
866 the GPS) or 0.003 (for the tremor, that is about 17 times the average

867 value of the signal). We mark by a blue rectangle every time where the
868 amplitude is lower than minus the threshold.

- 869 • Figure 6. Top: Stacked 7th level details of the wavelet decomposition of
870 the displacement over all the GPS stations located in a 50 km radius of a
871 given point, for the 16 red triangles indicated in Figure 3. Bottom: 7th
872 level detail multiplied by -1 of the cumulative tremor count in a 50 km
873 radius of a given point for the same 16 locations. The black lines represent
874 the timings of the ETS events from Table 1. We mark by a red rectangle
875 every time where the amplitude is higher than a threshold of 0.5 mm
876 (for the GPS) or 0.01 (for the tremor, that is about 56 times the average
877 value of the signal). We mark by a blue rectangle every time where the
878 amplitude is lower than minus the threshold.

- 879 • Figure 7. Top: Stacked 6th level details of the wavelet decomposition of
880 the displacement over all the GPS stations located in a 50 km radius of a
881 given point, for the 16 red triangles indicated in Figure 3. Bottom: 6th
882 level detail multiplied by -1 of the cumulative tremor count in a 50 km
883 radius of a given point for the same 16 locations. The black lines represent
884 the timings of the ETS events from Table 1. We mark by a red rectangle
885 every time where the amplitude is higher than a threshold of 0.3 mm (for
886 the GPS) or 0.009 (for the tremor, that is about 51 times the average
887 value of the signal). We mark by a blue rectangle every time where the
888 amplitude is lower than minus the threshold.

- 889 • Figure 8. ROC curve for the sum of the 6th, 7th, and 8th level details
890 of the wavelet decomposition. Each dot represents the true positive rate
891 of event detections and the false positive rate of event detections for a
892 given pair of thresholds (for the GPS and for the tremor). The black
893 cross marks the true positive rate and the false positive rate obtained

894 with the thresholds used to make Figure 9. The values of the threshold
895 are color-coded. Reds (bottom curve) correspond to the lowest value of
896 the threshold for the tremor (0.001), while oranges, greens, blues, purples
897 correspond to increasing values of the threshold for the tremor (up to 0.01,
898 top curve). The brightest colors (bottom left) correspond to the highest
899 values of the threshold for the GPS (1.5 mm), while the darker colors (top
900 right) correspond to decreasing values of the threshold for the GPS (0.1
901 mm).

- 902 • Figure 9. Top: Stacked sum of the 6th, 7th and 8th levels details of
903 the wavelet decomposition of the displacement over all the GPS stations
904 located in a 50 km radius of a given point, for the 16 red triangles indicated
905 in Figure 3. Bottom: Sum of the 6th, 7th and 8th levels detail multiplied
906 by -1 of the cumulative tremor count in a 50 km radius of a given point for
907 the same 16 locations. The black lines represent the timings of the ETS
908 events from Table 1. We mark by a red rectangle every time where the
909 amplitude is higher than a threshold of 0.8 mm (for the GPS) or 0.01 (for
910 the tremor, that is about 56 times the average value of the signal). We
911 mark by a blue rectangle every time where the amplitude is lower than
912 minus the threshold.
- 913 • Figure 10. Top: Stacked 5th level details of the wavelet decomposition
914 of the displacement over all the GPS stations located in a 50 km radius
915 of a given point, for the 16 red triangles indicated in Figure 3. The red
916 lines represent the timings of the ETS events from Table 1. The blue
917 lines represent the timings of the magnitude 5 events from the catalog of
918 Michel et al. (2019).
- 919 • Figure 11. Same as top panel of Figure 9: Stacked sum of the 6th, 7th
920 and 8th levels details of the wavelet decomposition of the displacement

921 over all the GPS stations located in a 50 km radius of a given point, for
922 the 16 red triangles indicated in Figure 3. We mark with a green bar the
923 slow slip events from Table 4 detected with the wavelet method. Full lines
924 correspond to robust detections (1 in Table 4) and dotted lines to less
925 robust detections (2 in Table 4).

- 926 • Figure 12. GPS stations used for the slow slip detection in New Zealand
927 (black triangles). The red triangles are the locations where we stack the
928 GPS data. They are located close to the 20 km depth contour of the plate
929 boundary from Williams et al. (2013).
- 930 • Figure 13. Top: Sum of the stacked 6th, 7th and 8th level details of
931 the wavelet decomposition of the displacement over all the GPS stations
932 located in a 50 km radius of a given point, for the 18 red triangles indicated
933 in Figure 12. The time period covered is 2010-2016. We mark by a red
934 rectangle every time where the amplitude is higher than a threshold equal
935 to 0.8 mm. We mark by a blue rectangle every time where the amplitude
936 is lower than minus the threshold. Bottom: Sum of the stacked 6th, 7th
937 and 8th level details of the wavelet decomposition. We mark with an
938 orange bar the slow slip events detected by Todd and Schwartz (2016)
939 and with a green bar the slow slip events from Table 5 detected with the
940 wavelet method. Full lines correspond to robust detections (1 in Table 5)
941 and dotted lines to less robust detections (2 in Table 5).
- 942 • Figure 14. Top: Sum of the stacked 6th, 7th and 8th level details of
943 the wavelet decomposition of the displacement over all the GPS stations
944 located in a 50 km radius of a given point, for the 18 red triangles indicated
945 in Figure 12. The time period covered in 2016-2022. We mark by a red
946 rectangle every time where the amplitude is higher than a threshold equal
947 to 0.8 mm. We mark by a blue rectangle every time where the amplitude

948 is lower than minus the threshold. We mark with a green bar the slow
949 slip events from Table 6 detected with the wavelet method. Full lines
950 correspond to robust detections (1 in Table 6) and dotted lines to less
951 robust detections (2 in Table 6).

₉₅₂ **Figures**

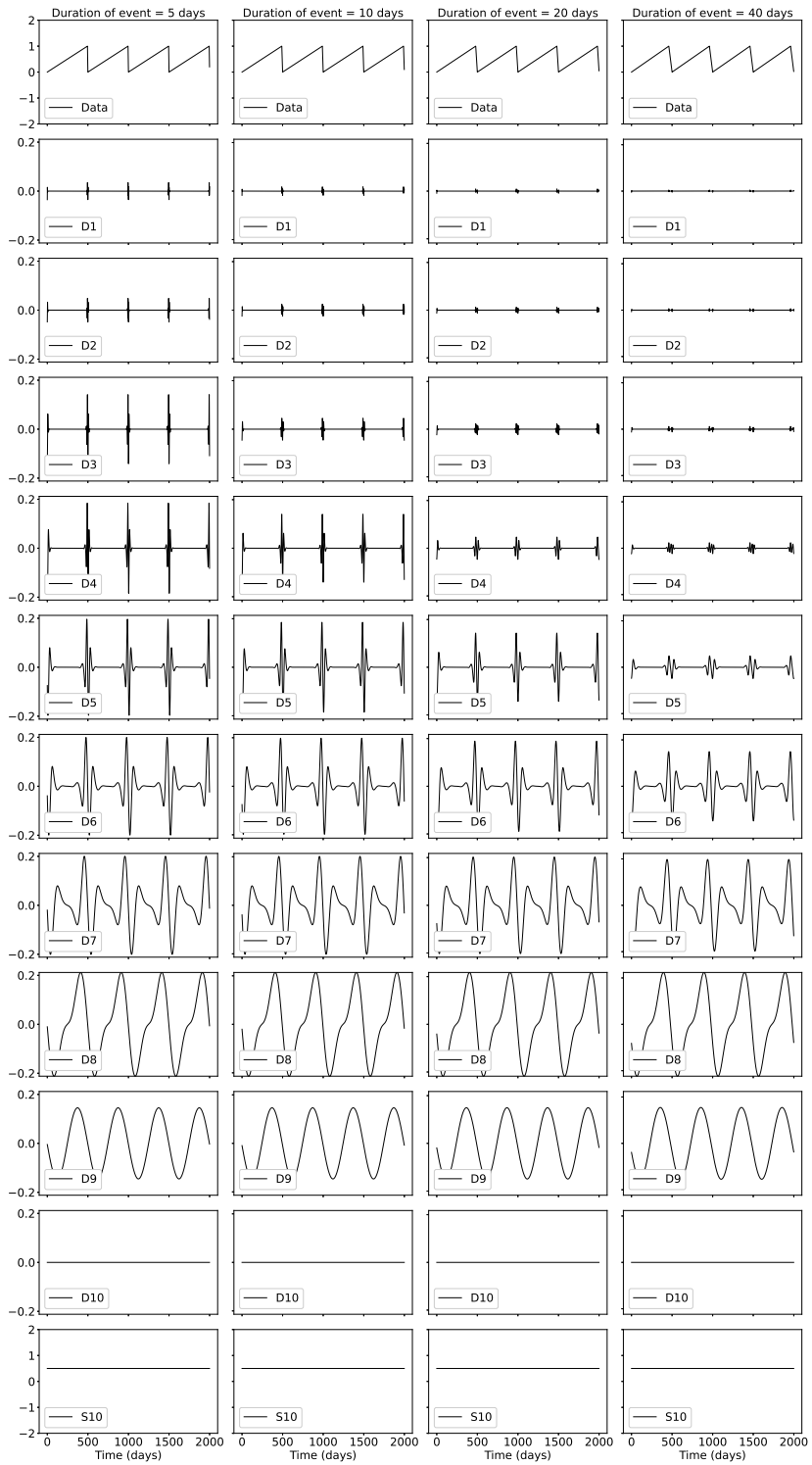


Figure 1: Demonstration of a wavelet decomposition for a synthetic dataset. A synthetic time series is created (top row) with steps of period 500 days, and transient durations of 2 days (left), 5 days, 10 days, and 20 days (right). The resulting details and smooths are shown in increasing level. The amplitude of the synthetic time series is normalized to 1, and the details and smooths show the relative amplitude. ⁴⁶

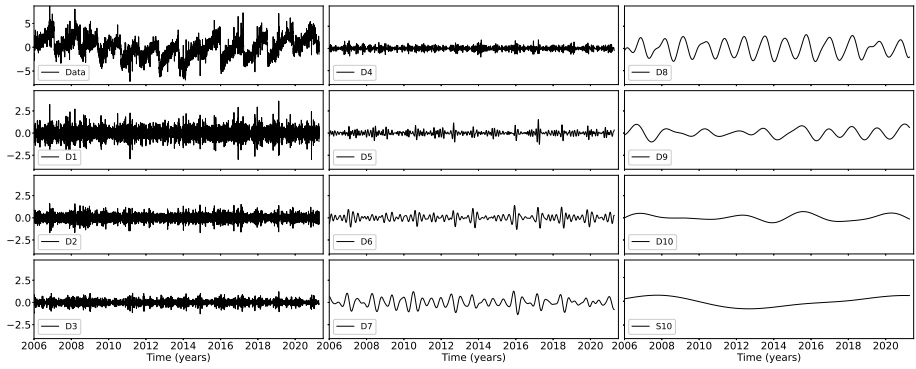


Figure 2: Top left: East-west displacement recorded at GPS station PGC5. The resulting details and smooth of the wavelet decomposition are shown in increasing level from top to bottom and from left to right.

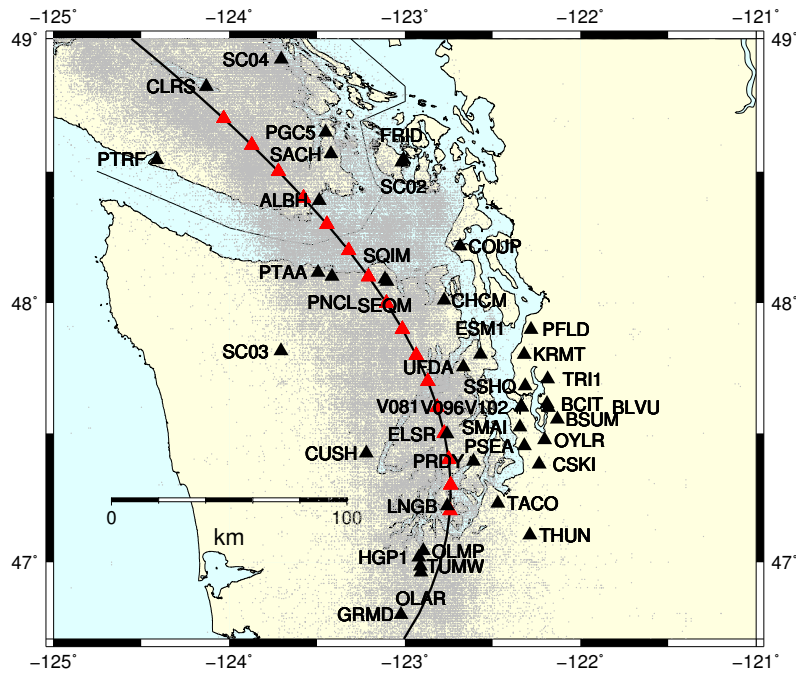


Figure 3: GPS stations used in this study (black triangles). The black line represents the 40 km depth contour of the plate boundary model by Preston et al. (2003). The red triangles are the locations where we stack the GPS data. The small grey dots are all the tremor locations from the PNSN catalog.

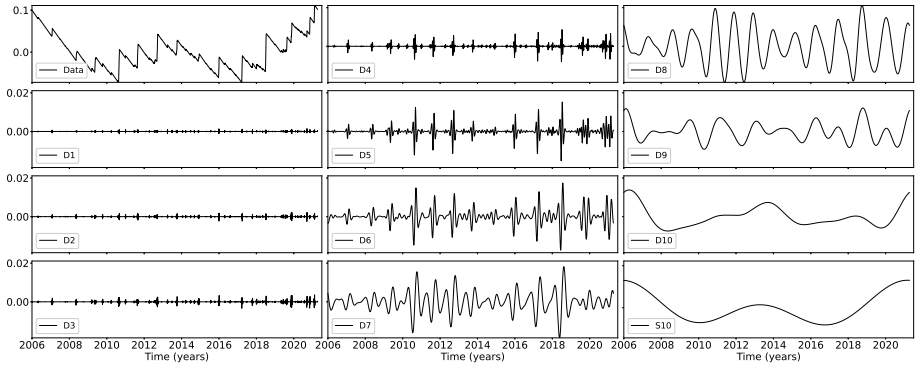


Figure 4: Details and smooth of the wavelet decomposition of the detrended cumulative tremor count around the third northernmost red triangles on Figure 3 (latitude 48.5).

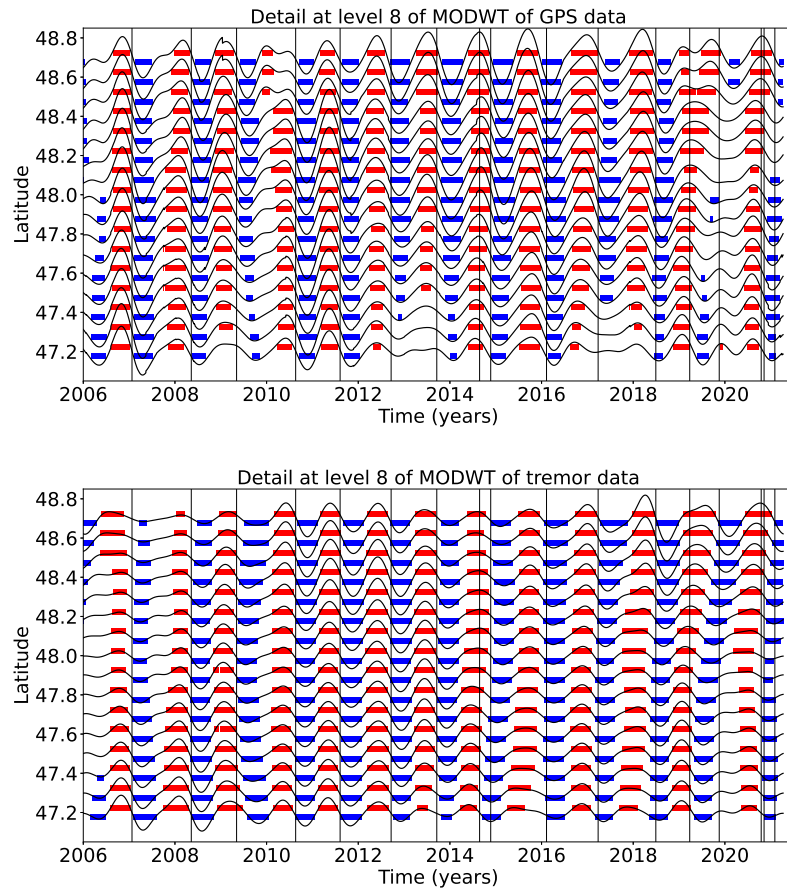


Figure 5: Top: Stacked 8th level details of the wavelet decomposition of the displacement over all the GPS stations located in a 50 km radius of a given point, for the 16 red triangles indicated in Figure 3. Bottom: 8th level detail multiplied by -1 of the cumulative tremor count in a 50 km radius of a given point for the same 16 locations. The black lines represent the timings of the ETS events from Table 1. We mark by a red rectangle every time where the amplitude is higher than a threshold of 0.4 mm (for the GPS) or 0.003 (for the tremor, that is about 17 times the average value of the signal). We mark by a blue rectangle every time where the amplitude is lower than minus the threshold.

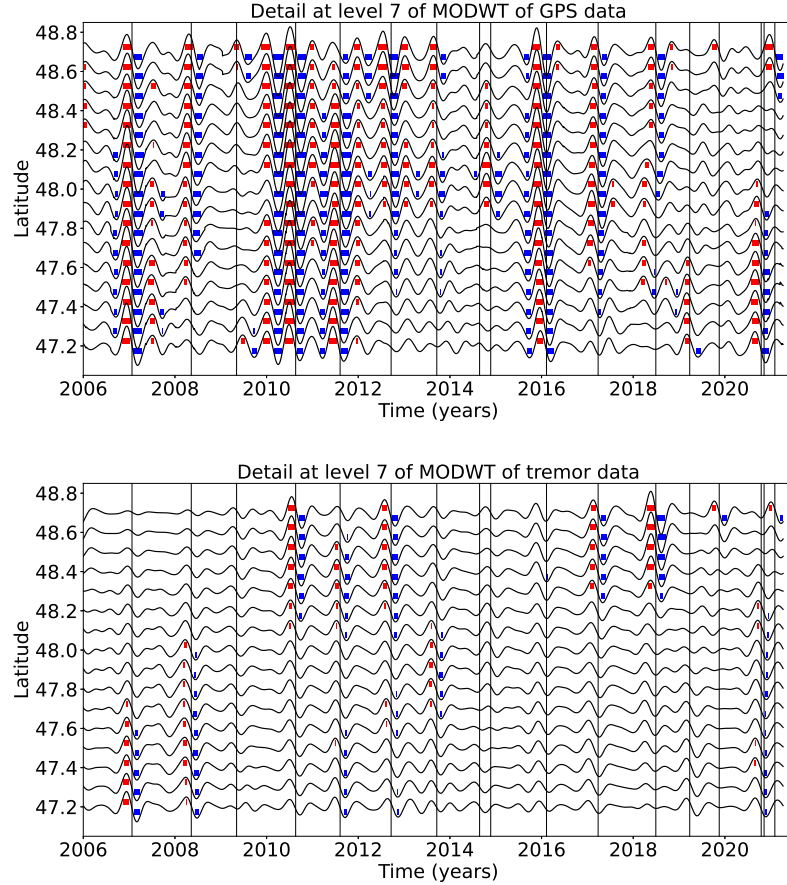


Figure 6: Top: Stacked 7th level details of the wavelet decomposition of the displacement over all the GPS stations located in a 50 km radius of a given point, for the 16 red triangles indicated in Figure 3. Bottom: 7th level detail multiplied by -1 of the cumulative tremor count in a 50 km radius of a given point for the same 16 locations. The black lines represent the timings of the ETS events from Table 1. We mark by a red rectangle every time where the amplitude is higher than a threshold of 0.5 mm (for the GPS) or 0.01 (for the tremor, that is about 56 times the average value of the signal). We mark by a blue rectangle every time where the amplitude is lower than minus the threshold.

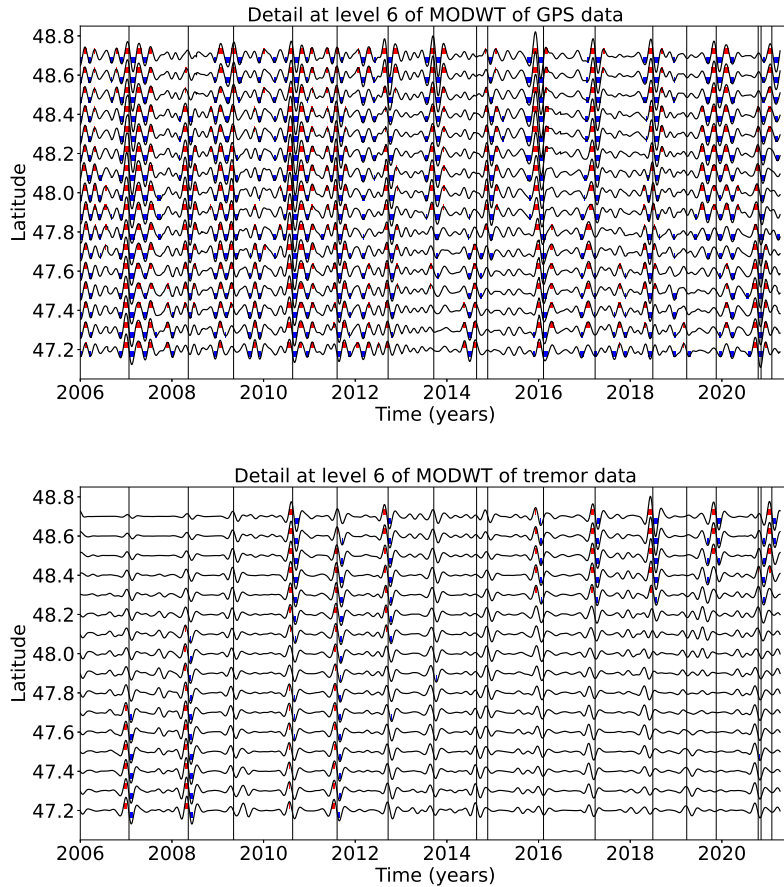


Figure 7: Top: Stacked 6th level details of the wavelet decomposition of the displacement over all the GPS stations located in a 50 km radius of a given point, for the 16 red triangles indicated in Figure 3. Bottom: 6th level detail multiplied by -1 of the cumulative tremor count in a 50 km radius of a given point for the same 16 locations. The black lines represent the timings of the ETS events from Table 1. We mark by a red rectangle every time where the amplitude is higher than a threshold of 0.3 mm (for the GPS) or 0.009 (for the tremor, that is about 51 times the average value of the signal). We mark by a blue rectangle every time where the amplitude is lower than minus the threshold.

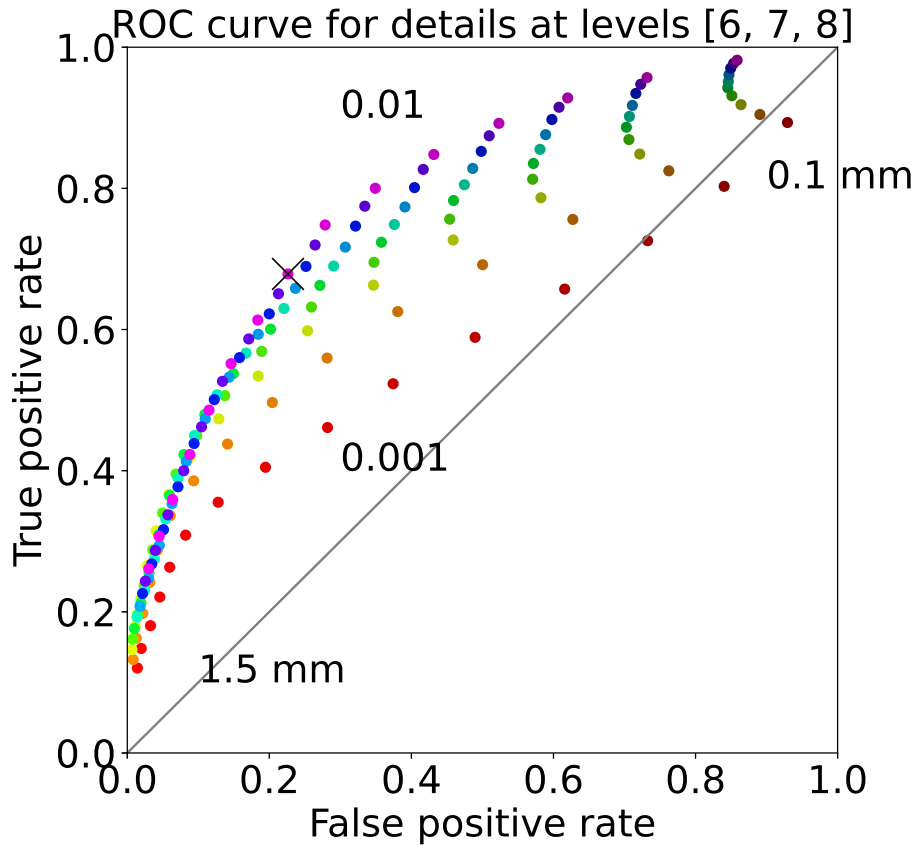


Figure 8: ROC curve for the sum of the 6th, 7th, and 8th level details of the wavelet decomposition. Each dot represents the true positive rate of event detections and the false positive rate of event detections for a given pair of thresholds (for the GPS and for the tremor). The black cross marks the true positive rate and the false positive rate obtained with the thresholds used to make Figure 9. The values of the threshold are color-coded. Reds (bottom curve) correspond to the lowest value of the threshold for the tremor (0.001), while oranges, greens, blues, purples correspond to increasing values of the threshold for the tremor (up to 0.01, top curve). The brightest colors (bottom left) correspond to the highest values of the threshold for the GPS (1.5 mm), while the darker colors (top right) correspond to decreasing values of the threshold for the GPS (0.1 mm).

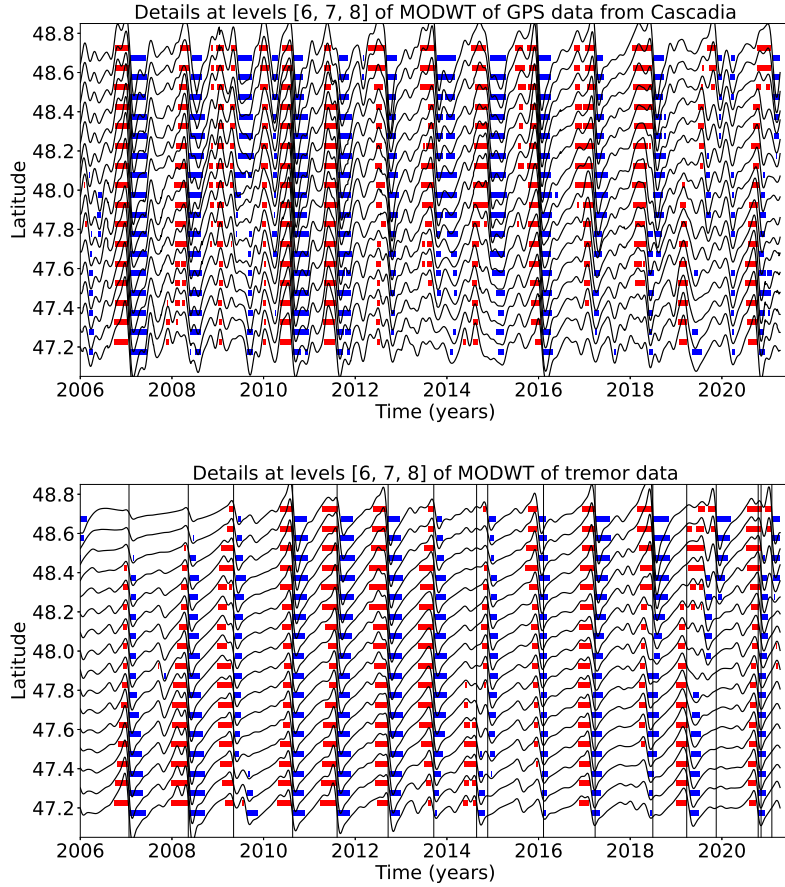


Figure 9: Top: Stacked sum of the 6th, 7th and 8th levels details of the wavelet decomposition of the displacement over all the GPS stations located in a 50 km radius of a given point, for the 16 red triangles indicated in Figure 3. Bottom: Sum of the 6th, 7th and 8th levels detail multiplied by -1 of the cumulative tremor count in a 50 km radius of a given point for the same 16 locations. The black lines represent the timings of the ETS events from Table 1. We mark by a red rectangle every time where the amplitude is higher than a threshold of 0.8 mm (for the GPS) or 0.01 (for the tremor, that is about 56 times the average value of the signal). We mark by a blue rectangle every time where the amplitude is lower than minus the threshold.

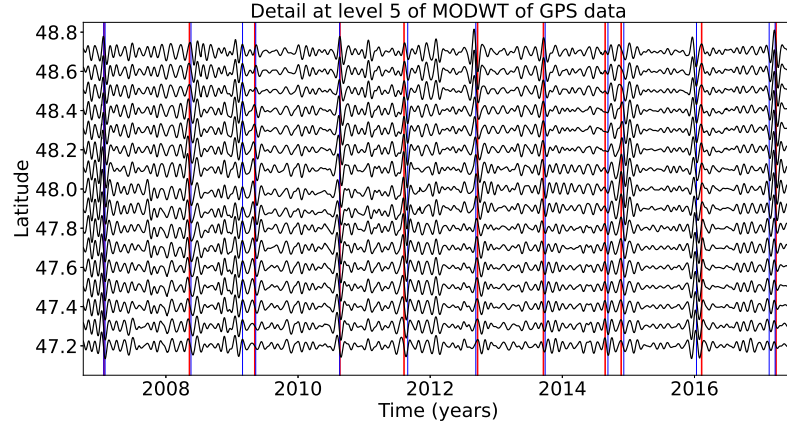


Figure 10: Top: Stacked 5th level details of the wavelet decomposition of the displacement over all the GPS stations located in a 50 km radius of a given point, for the 16 red triangles indicated in Figure 3. The red lines represent the timings of the ETS events from Table 1. The blue lines represent the timings of the magnitude 5 events from the catalog of Michel et al. (2019).

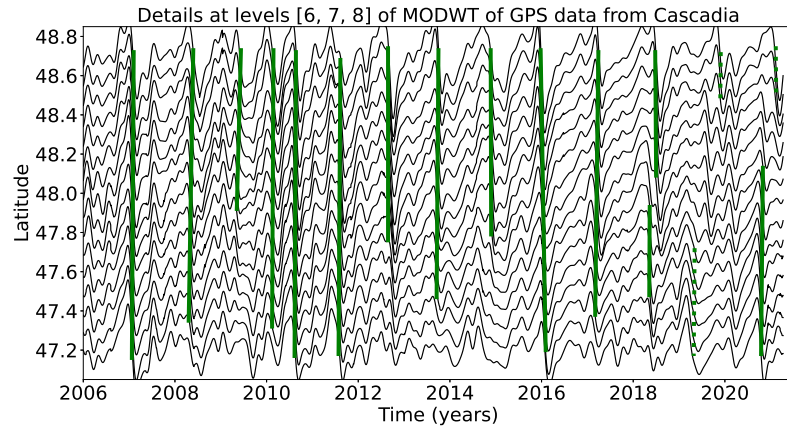


Figure 11: Same as top panel of Figure 9: Stacked sum of the 6th, 7th and 8th levels details of the wavelet decomposition of the displacement over all the GPS stations located in a 50 km radius of a given point, for the 16 red triangles indicated in Figure 3. We mark with a green bar the slow slip events from Table 4 detected with the wavelet method. Full lines correspond to robust detections (1 in Table 4) and dotted lines to less robust detections (2 in Table 4).

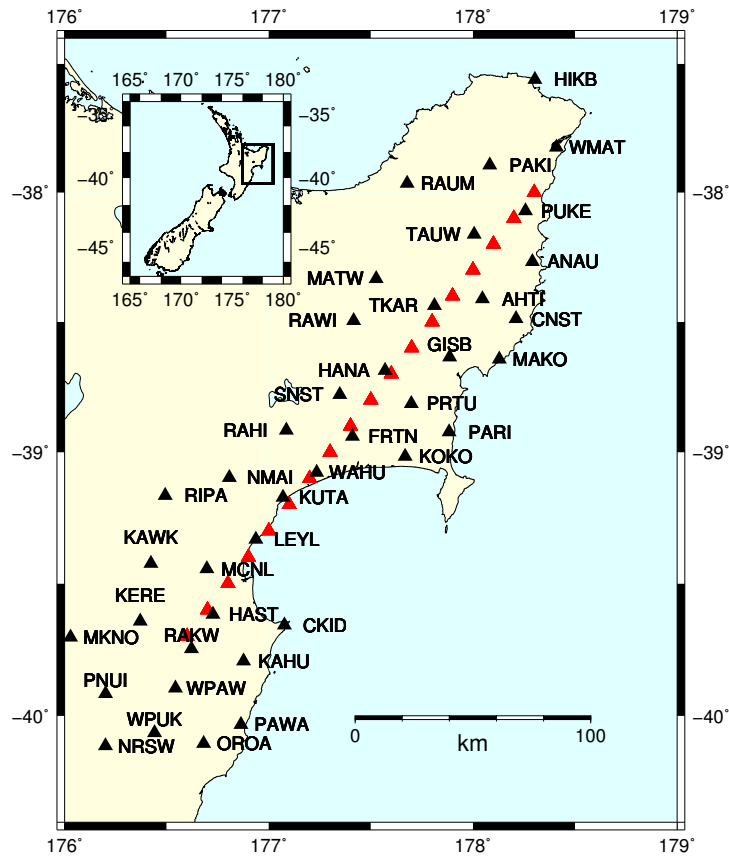


Figure 12: GPS stations used for the slow slip detection in New Zealand (black triangles). The red triangles are the locations where we stack the GPS data. They are located close to the 20 km depth contour of the plate boundary from Williams et al. (2013).

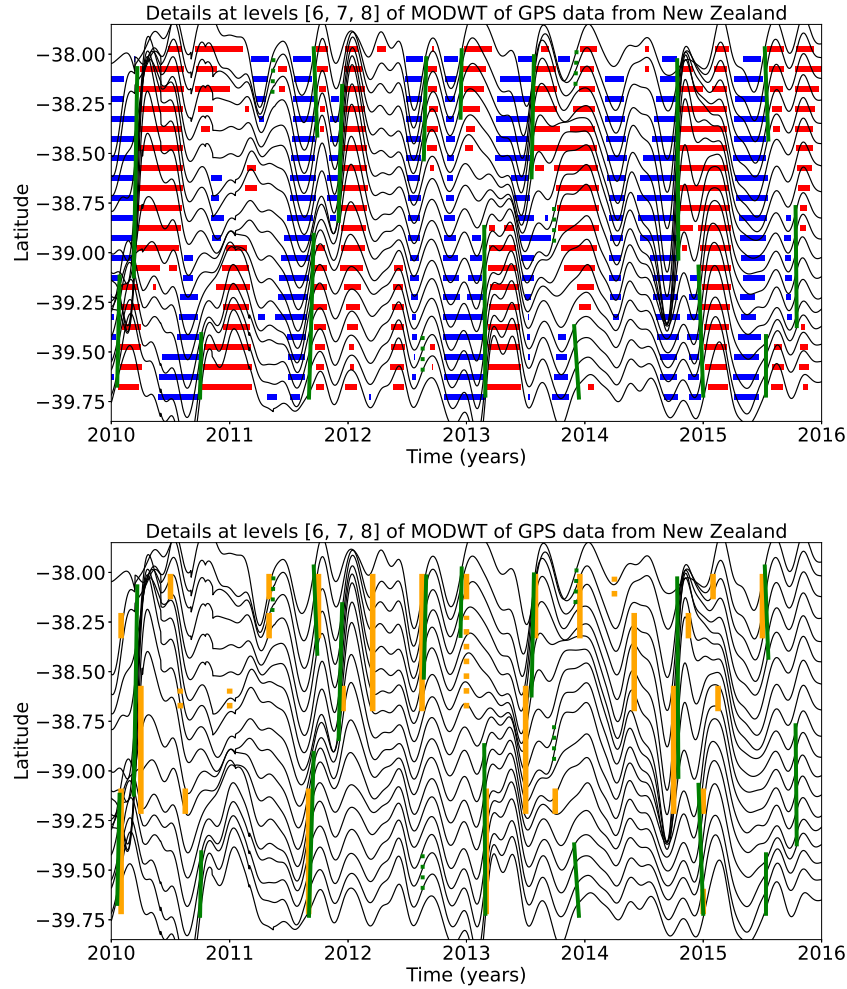


Figure 13: Top: Sum of the stacked 6th, 7th and 8th level details of the wavelet decomposition of the displacement over all the GPS stations located in a 50 km radius of a given point, for the 18 red triangles indicated in Figure 12. The time period covered is 2010-2016. We mark by a red rectangle every time where the amplitude is higher than a threshold equal to 0.8 mm. We mark by a blue rectangle every time where the amplitude is lower than minus the threshold. Bottom: Sum of the stacked 6th, 7th and 8th level details of the wavelet decomposition. We mark with an orange bar the slow slip events detected by Todd and Schwartz (2016) and with a green bar the slow slip events from Table 5 detected with the wavelet method. Full lines correspond to robust detections (1 in Table 5) and dotted lines to less robust detections (2 in Table 5).

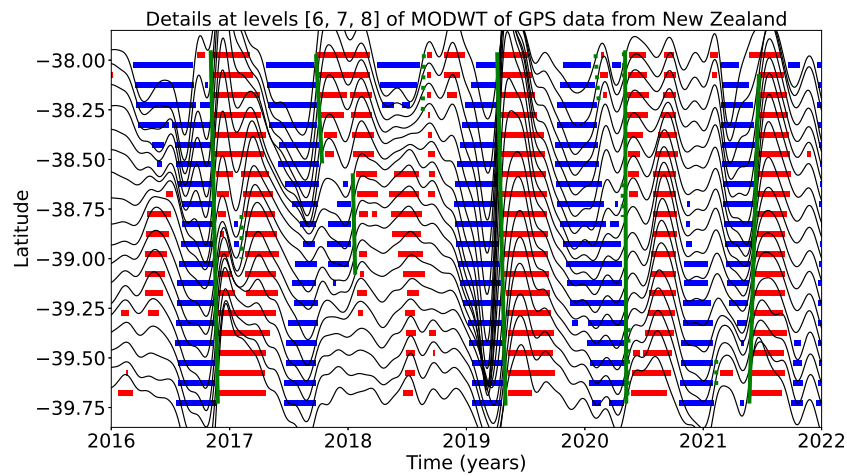


Figure 14: Top: Sum of the stacked 6th, 7th and 8th level details of the wavelet decomposition of the displacement over all the GPS stations located in a 50 km radius of a given point, for the 18 red triangles indicated in Figure 12. The time period covered in 2016-2022. We mark by a red rectangle every time where the amplitude is higher than a threshold equal to 0.8 mm. We mark by a blue rectangle every time where the amplitude is lower than minus the threshold. We mark with a green bar the slow slip events from Table 6 detected with the wavelet method. Full lines correspond to robust detections (1 in Table 6) and dotted lines to less robust detections (2 in Table 6).